Check for updates



ADVANCED FUNCTIONAL MATERIALS
www.afm-journal.de

# Improving the Efficiency of Gallium Telluride for Photocatalysis, Electrocatalysis, and Chemical Sensing through Defects Engineering and Interfacing with its Native Oxide

*Federica Bondino,* Songül Duman, Silvia Nappini, Gianluca D'Olimpio, Corneliu Ghica, Tevfik Onur Menteş, Federico Mazzola, Marian Cosmin Istrate, Matteo Jugovac, Mykhailo Vorokhta, Sergio Santoro, Bekir Gürbulak, Andrea Locatelli, Danil W. Boukhvalov, and Antonio Politano**

**Gallium telluride (GaTe) is a van der Waals semiconductor, currently adopted for photonic and optoelectronic devices. However, the rapid degradation of GaTe in air, promoted by Te vacancies, is detrimental for device applications. Here, it is demonstrate that the surface oxidation of GaTe can be unexpectedly exploited for expanding the breadth of applications of GaTe. Specifically, the formation of a nanoscale sub-stoichiometric wide-band-gap $Ga_2O_3$ skin, promoted by Te vacancies, over narrow-band-gap $GaTe_x$ upon air exposure is beneficial for electrocatalysis, photocatalysis, and gas sensing . In particular, the Heyrovsky step ($H_{ads} + H^+ + e^- \rightarrow H_2$) of hydrogen evolution reaction in an acidic medium is barrier-free for the sub-stoichiometric gallium-oxide/gallium-telluride heterostructure, which also enables a significant reduction of costs with respect to state-of-the-art Pt/C electrodes. In the photocatalytic process, the photo-generated electrons migrate from GaTe to $Ga_2O_x$ skin, which acts as the chemically active side of the interface. Moreover, the $Ga_2O_3$/GaTe heterostructure is a suitable platform for sensing of $H_2O$, $NH_3$, and $NO_2$ at operational temperatures extended up to 600 °C (useful for gas detection in combustion processes), mainly due to the increased area of charge redistribution after adsorption achieved upon oxidation of GaTe.**

## 1. Introduction

Among the atlas of 2D materials, van der Waals (vdW) semiconductors deserve particular attention,[1] considering their complementarity with respect to the forefather of 2D materials, i.e., graphene,[2] lacking a band gap.[3] Transition-metal dichalcogenides (e.g., $MoS_2$,[4] $MoSe_2$,[5] $MoTe_2$,[6] $WS_2$,[7] $WSe_2$[8]) show a band gap energy depending on thickness, which turns out to be direct only in the monolayer. Nevertheless, the isolation of a single layer represents a rather complicated challenge, bearing in mind that i) mechanical exfoliation fails in scalability, ii) liquid-phase exfoliation yields flakes with multilayer thickness, and iii) epitaxial growth does not produce stoichiometric samples, owing to the presence of a copious amount of chalcogen vacancies, inevitably altering electronic and physicochemical properties. Hence, a vdW semiconductor showing a

F. Bondino, S. Nappini, F. Mazzola
Consiglio Nazionale delle Ricerche (CNR)- Istituto Officina dei Materiali (IOM)
Area Science Park S.S. 14 km 163.5, Trieste 34149, Italy
E-mail: bondino@iom.cnr.it

S. Duman
Basic Sciences Department
Faculty of Sciences
Erzurum Technical University
Erzurum 25050, Turkey

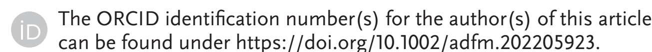
The ORCID identification number(s) for the author(s) of this article can be found under https://doi.org/10.1002/adfm.202205923.

© 2022 The Authors. Advanced Functional Materials published by Wiley-VCH GmbH. This is an open access article under the terms of the Creative Commons Attribution-NonCommercial License, which permits use, distribution and reproduction in any medium, provided the original work is properly cited and is not used for commercial purposes.

**DOI: 10.1002/adfm.202205923**

G. D'Olimpio, A. Politano
Department of Physical and Chemical Sciences
University of L'Aquila
via Vetoio, L'Aquila (AQ) 67100, Italy
E-mail: antonio.politano@univaq.it

C. Ghica, M. C. Istrate
National Institute of Materials Physics
Atomistilor 405A, Magurele 077125, Romania

T. O. Menteş, M. Jugovac, A. Locatelli
Elettra-Sincrotrone S.C.p.A
S.S. 14-km 163.5 in AREA Science Park, Trieste 34149, Italy

M. Vorokhta
Charles University
V Holešovičkách 2, Prague 8, Prague 18000, Czech Republic

S. Santoro
Department of Environmental Engineering (DIAM)
University of Calabria
Via Pietro Bucci cubo 44A, Rende (CS) 87036, Italy

16163028, 2022, 41, Downloaded from https://onlinelibrary.wiley.com/doi/10.1002/adfm.202205923 by CNR GROUP II Istituto di Scienza dell', Wiley Online Library on [23/05/2024]. See the Terms and Conditions (https://onlinelibrary.wiley.com/terms-and-conditions) on Wiley Online Library for rules of use; OA articles are governed by the applicable Creative Commons License

direct band gap already in the bulk would be highly desirable. A good candidate for such aims is represented by gallium telluride (GaTe), which crystallizes in a monoclinic structure (space group B2/m) with Te-Ga-Ga-Te stacking.[9] Remarkably, GaTe possesses a direct band gap, which varies from 1.60 eV in the bulk to 1.67 eV for monolayer at room temperature.[10] Furthermore, GaTe provides further advantages related to its in-plane anisotropy, mirrored in its anisotropic optical properties.[11] Compared to its parental compounds (as GaSe and GaS), GaTe displays higher absorptivity[12] with superior potential for applications in nonlinear optics.[13] GaTe photodetectors combine outstanding responsivity ($10^4$ A $W^{-1}$) with fast photoresponse (6 ms)[14] and high detectivity ($10^{12}$ Jones).[10] Moreover, both nanowires and nanosheets of GaTe are promising candidates for sunlight-driven photocatalysis[15] (especially, water splitting[16]), and flexible photodetectors[17] (also in the ultraviolet[18]).

However, the growth of large-size, highly crystalline bulk GaTe crystals is particularly complex, due to the presence of solid-state phase transitions and the more complicated crystal structure than parental Ga chalcogenides.[19] Furthermore, the poor environmental stability of GaTe,[17a,20] with oxidation starting in a timescale of two hours up to a completely oxidized GaTe layer after one week in air,[21] represents a hurdle for the industrial exploitation of GaTe-based devices. Accordingly, encapsulation strategies have been recently devised in order to protect active channels in nanodevices,[20b,c,21,22] although their complexity (encapsulation with graphene,[21] hexagonal boron nitride (h-BN)[23] or $Al_2O_3$,[22] passivation with ultrathin hydrogen–silsesquioxane film,[24] surface functionalization with diazonium molecules[25]) could be unsuitable for industrial applications.

Another important aspect is related to the impact of defects on physicochemical properties. Actually, defects engineering could provide further functionalities to GaTe-based applications. As a matter of fact, the presence of defect sites in GaTe nanomaterials was correlated to the observation of narrow and bright photoluminescence at energies well below the optical band gap.[26] Specifically, the deviation from stoichiometry could be used to tailor the efficiency of GaTe-based applications in optoelectronics. Especially, Ga-rich GaTe ($GaTe_{1-|x|}$) displays higher carrier mobility, carrier lifetime, and resistivity compared to Te-rich GaTe ($Ga_{1-|x|}Te$) for radiation detection applications,[27] while Ga vacancies are detrimental to the performance of GaTe-based field-effect transistors.[28]

Here, we demonstrate, by a combination of surface-science techniques, complemented by density functional theory (DFT), that the inevitable oxidation of GaTe in the ambient atmosphere (driven by Te vacancies) induces the formation of a $Ga_2O_3$/GaTe heterostructure with drastically different performance in i) electrocatalysis (namely, hydrogen evolution reaction, HER), ii) photocatalysis, iii) and gas sensing. In particular, the Heyrovsky step ($H_{ads} + H^+ + e^- \rightarrow H_2$) of HER in an acidic medium is barrier-free for the sub-stoichiometric gallium-oxide/gallium-telluride heterostructure, which also enables a significant reduction of costs by 160 times with respect to state-of-the-art Pt/C electrodes. Moreover, in photocatalytic processes, the generation of electron-hole pairs occurs at the underlying GaTe bulk, whereas catalytic reactions occur at active sites of the $Ga_2O_3$ skin. Thus, the natural interaction of metal chalcogenides toward the ambient gases could be exploited in photocatalysis, where the underlying vdW semiconductor (GaTe) provides electron-hole pair, while O-vacancy sites of the $Ga_2O_3$ skin formed upon oxidation represent the active sites for catalytic reactions. Finally, we prove that the $Ga_2O_3$/GaTe heterostructure is a suitable platform for sensing of water($H_2O$), ammonia ($NH_3$), and nitrogen dioxide ($NO_2$) at operational temperatures extended up to 600 °C (useful for identification and detection of gaseous species in combustion processes), mainly due to the increased area of charge redistribution after adsorption achieved upon surface oxidation of GaTe.

B. Gürbulak
Department of Physics
Faculty of Sciences
Atatürk University
Erzurum 25240, Turkey
D. W. Boukhvalov
College of Science
Institute of Materials Physics and Chemistry
Nanjing Forestry University
Nanjing 210037, P. R. China

## 2. Results and Discussion

### 2.1. Surface Structure and Electronic Band Structure of GaTe

The surface properties of GaTe remain far from comprehension. Previously, surface phase transitions were evidenced by scanning tunneling microscopy and spectroscopy (STM/STS), low-energy electron diffraction (LEED),[29] and transmission electron microscopy (TEM).[30] In particular, a partial reconstruction from monoclinic to hexagonal was observed in the LEED pattern after cleaving the sample in an ultra-high vacuum (UHV).[29b]

The use of low-energy electron microscopy (LEEM), and, more explicitly, μ-LEED, could provide unambiguous information on this issue, owing to the superior surface sensitivity. Our μ-LEED experiments indicate the presence of a monoclinic structure (**Figure 1**c), congruent with the unit cell depicted in Figure 1b. Importantly, at certain electron energies, some diffraction spots appear more pronounced tracing out an apparently hexagonal pattern with three-fold symmetry, exactly as in Ref. [29b], where authors claimed the presence of a phase transition. Nevertheless, their interpretation looks inappropriate, considering that our own nanospectroscopy and spatially resolved diffraction experiments indicate the only presence of monoclinic phase in samples cleaved in UHV conditions, contrary to conclusions in Ref. [29b]. Further support for this picture is provided by the analysis of angle-resolved photoemission spectroscopy (ARPES) data (**Figure 2**), fully matching with a monoclinic phase. The experimental band structure shows a well-defined valence band dispersing over the entire Brillouin zone, with a maximum located at the Γ point. At ~1.5 eV from the valence-band maximum, a second hole-like parabolic dispersion is also visible.


© 2022 The Authors. Advanced Functional Materials published by Wiley-VCH GmbH

16163028, 2022, 41, Downloaded from https://onlinelibrary.wiley.com/doi/10.1002/adfm.202205923 by CNR GROUP II Istituto di Scienza dell', Wiley Online Library on [23/05/2024]. See the Terms and Conditions (https://onlinelibrary.wiley.com/terms-and-conditions) on Wiley Online Library for rules of use; OA articles are governed by the applicable Creative Commons License

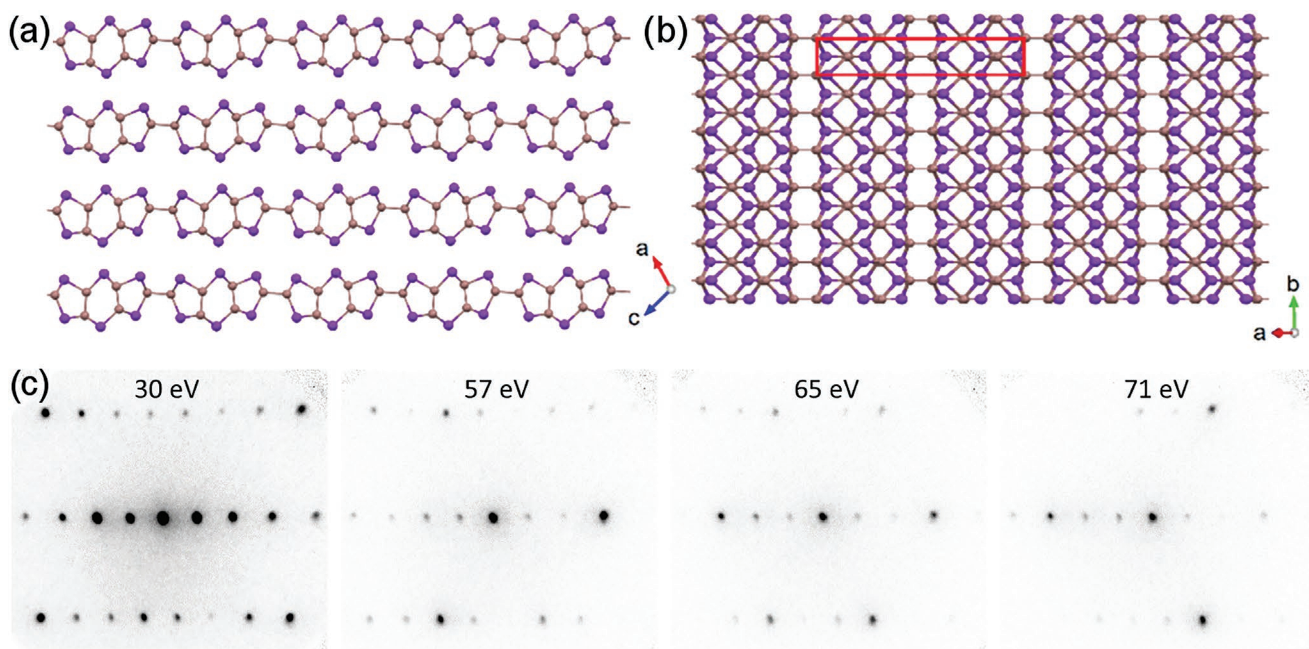


**Figure 1.** View of monoclinic GaTe in a) side and b) top views. Gallium and tellurium atoms are depicted in brown and violet, respectively. The in-plane rectangular unit cell is represented on panel (b) in red. c) µ-LEED patterns observed at different electron energies.

### 2.2. Chemical Reactivity of Surfaces of Pristine and Defective GaTe

Theoretical modeling (see Methods for more details) can display the key features of the chemical stability of GaTe in both liquid phase and air. Specifically, the calculated interlayer binding energy of GaTe (8.68 kJ $mol^{-1}$) is rather small, as expected from the monoclinic atomic structure (Figure 1; see also Figure S1 in the Supporting Information), in which only $^1/_3$ Te atoms participate in the formation of interlayer bonds. The energy required for the removal of Te atoms from the surface of GaTe is 73.33 and 39.56 kJ/Te for bulk and monolayer GaTe, respectively. Moreover, the energy for vacancy formation in the monolayer is almost twice smaller than in the bulk, proving the notable contribution from the local distortion of the flexible monolayer GaTe in the energetics of defects formation. Accordingly, a significant number of anionic vacancies in GaTe samples (both bulk and monolayer) unavoidably exists. Consequently, a reliable assessment of physicochemical properties, including chemical reactivity and (photo)electrocatalytic activity, should carefully account for the influence of defects in monoclinic GaTe, though such a relevant issue has never been addressed to date.

We modeled the energetics of adsorption of ambient gases,water and oxygen ($O_2$), on defective and defect-free

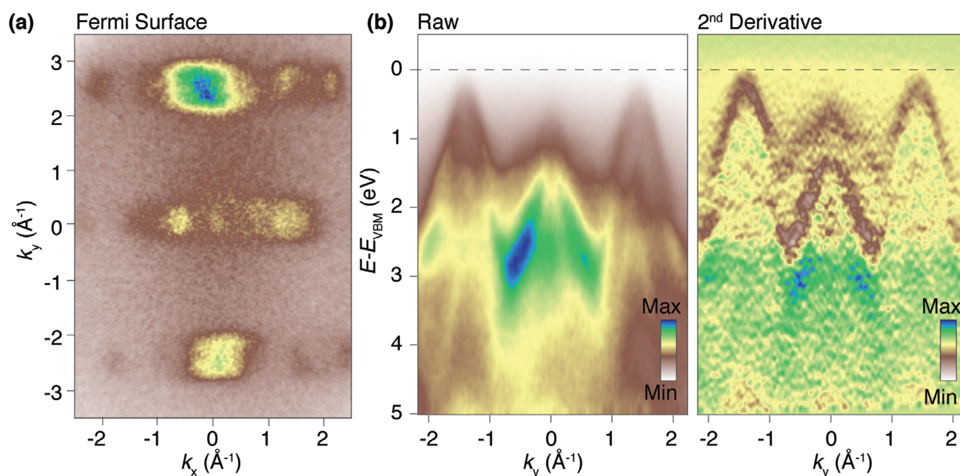


**Figure 2.** a) Constant energy $k_x$-$k_y$ cutting through the valence-band edge of GaTe. b) Raw and c) second derivative of the valence-band structure collected at 94 eV photon energy. Photon polarization is 16 degrees off the surface normal. The valence band top in the first Brillouin zone is suppressed by the matrix elements but recovered in the second zone. The energy scale was set to zero the valence-band maximum (VBM).

 © 2022 The Authors. Advanced Functional Materials published by Wiley-VCH GmbH

16163028, 2022, 41, Downloaded from https://onlinelibrary.wiley.com/doi/10.1002/adfm.202205923 by CNR GROUP II Istituto di Scienza dell', Wiley Online Library on [23/05/2024]. See the Terms and Conditions (https://onlinelibrary.wiley.com/terms-and-conditions) on Wiley Online Library for rules of use; OA articles are governed by the applicable Creative Commons License

**Table 1.** Energetics of adsorption on defective and defect-free surfaces of bulk and monolayer GaTe. Energies of the oxidation of whole surfaces (Figure 3c) are reported in parenthesis.

| Structure | Substrate | Adsorbant | Physisorption | | Decomposition $\Delta H_{dec}$ [kJ mol$^{-1}$] |
|---|---|---|---|---|---|
| | | | $\Delta H_{ads}$ [kJ mol$^{-1}$] | $\Delta G$ [kJ mol$^{-1}$] | |
| bulk | GaTe | $O_2$ | −73.38 | −61.89 | −141.27 (+14.22) |
| | | $H_2O$ | −144.13 | −112.83 | +127.36 |
| | $GaTe_{0.97}$ | $O_2$ | −55.81 | −44.32 | −282.19 (−35.53) |
| | | $H_2O$ | −27.42 | +3.38 | −151.47 |
| monolayer | GaTe | $O_2$ | +69.92 | +81.41 | −128.77 (−77.54) |
| | | $H_2O$ | +39.10 | +70.45 | +356.25 |
| | $GaTe_{0.97}$ | $O_2$ | dissociative ads. | – | −568.20 (−17.53) |
| | | $H_2O$ | dissociative ads. | – | −241.16 |

surfaces of bulk and monolayer GaTe (**Table 1**). Explicitly, physisorption of water at room temperature on the surface of the bulk crystal is favorable on defect-free GaTe ($\Delta G$ = −112.83 kJ mol$^{-1}$) and metastable on Te-vacancy sites (+3.38 kJ mol$^{-1}$ in $GaTe_{0.97}$). Decomposition of water molecules is strongly unfavorable (+127.36 kJ mol$^{-1}$) in defect-free areas of GaTe surface and favorable in the presence of Te vacancies (−151.47 kJ mol$^{-1}$ in $GaTe_{0.97}$). On the other hand, the energy of the intercalation of water molecules between the layers is rather energetically favorable (−104.30 kJ mol$^{-1}$). Note that the presence of water in the interlayer space leads to a distortion of GaTe layers (see Figure S2, Supporting Information), which could provide further collapse of a layered structure with a phase transition from monoclinic to cubic. Water decomposition on Te vacancies of cubic GaTe (Figure S3, Supporting Information) is energetically favorable (−32.94 kJ mol$^{-1}$). Thus, bulk GaTe cannot be considered as a suitable platform for catalysis in liquid media.

Whenever the thickness of the GaTe sample is reduced to the monolayer regime, water decomposition is highly favored in the presence of Te vacancies (−241.16 kJ mol$^{-1}$). Considering the obvious abundance of anionic defects in GaTe nanosheets produced by liquid-phase exfoliation, the instability of GaTe monolayers in liquid media is practically unavoidable.

In oxidative environments (including air), robust oxygen physisorption (**Figure 3**a) with further decomposition (Figure 3b) occurs on both defects-free and defective surfaces of bulk GaTe crystals. Precisely, $\Delta G$ values for physisorption and decomposition of oxygen are −61.89 and −141.27 kJ mol$^{-1}$ for GaTe and −44.32 and −282.19 kJ mol$^{-1}$ for $GaTe_{0.97}$, respectively. Thus, 3% Te vacancies are able to nearly double the decomposition energy for oxygen molecules at room temperature. Therefore, the scenario of an energy gap tuning in GaTe by molecular oxygen intercalation recently suggested[20d] cannot be realized, considering that oxygen forms covalent bonds with GaTe.

The oxygenation of Te atoms in the outermost surface layer evolves into the formation of a tellurium-dioxide layer (Figure 3c), which is an extremely favorable exothermic process. However, the structure shown in Figure 3b is also unstable (see below) and it is transformed into a $Ga_2O_3$ skin. Precisely, the formation of a $Ga_2O_3$ skin and Te(0) phases from the full oxidation of GaTe (Figure 3c) can be described as:

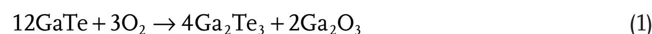

$$12GaTe + 3O_2 \rightarrow 4Ga_2Te_3 + 2Ga_2O_3 \quad (1)$$

$$2Ga_2Te_3 + 3O_2 \rightarrow 2Ga_2O_3 + 6Te \quad (2)$$

and

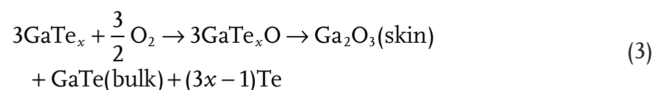

$$3GaTe_x + \frac{3}{2}O_2 \rightarrow 3GaTe_xO \rightarrow Ga_2O_3(skin) + GaTe(bulk) + (3x-1)Te \quad (3)$$

These reaction paths involve the formation of $Ga_2Te_3$ and $GaTe_xO$ as intermediate steps and the formation of atomic tellurium. Definitely, atomic tellurium passivates Te vacancies in sub-surface layers of $GaTe_x$ and, subsequently, tellurium oxides (TeO, $TeO_2$, and $TeO_3$) could be formed in oxygen-rich environments. All the above-mentioned processes are exothermic with rather large magnitudes of enthalpy (−844 kJ/$Ga_2O_3$, −170 kJ/TeO, −494 kJ/$TeO_2$, and −673 kJ/$TeO_3$ unit cell, respectively). In the case of a defect-free GaTe monolayer, the energy cost for the distortion of the membrane (≈152 kJ per cell) overcomes the energy gain from the physisorption of molecular oxygen.

To validate theoretical predictions, we carried out a surface-science investigation on the chemical reactivity of GaTe by i) near-ambient pressure photoemission spectroscopy (NAP-XPS), complemented by synchrotron-based high-resolution X-ray photoelectron spectroscopy (XPS) and X-ray photoemission electron microscopy (XPEEM) using soft X-ray photons to enhance surface sensitivity and photoionization cross-sections. Measurements were performed using high-quality single crystals (Figure S1, Supporting Information), grown through an

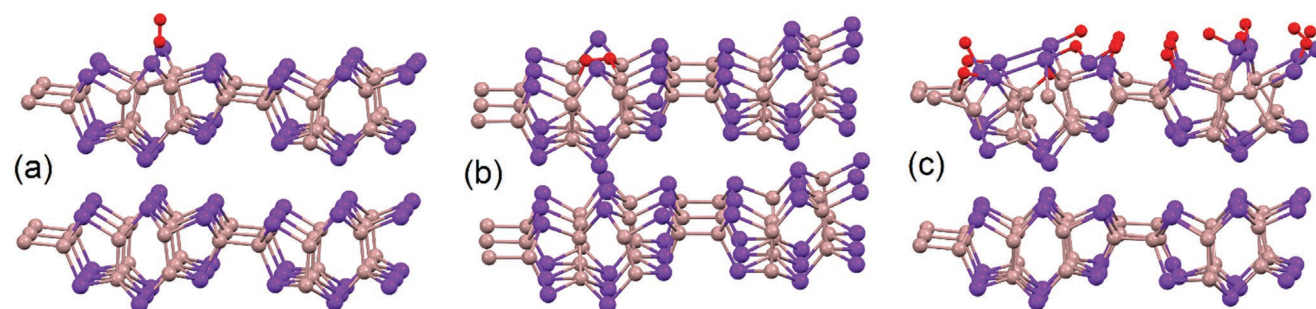


**Figure 3.** Optimized atomic structures of a) molecular oxygen physisorption and b) further decomposition on the surface of $GaTe_{0.97}$ bulk crystal. c) Optimized atomic structure of the initial state of the formation of oxide layer on the surface of $GaTe_{0.97}$ bulk crystal. Oxygen atoms are depicted in red.


© 2022 The Authors. Advanced Functional Materials published by Wiley-VCH GmbH

16163028, 2022, 41, Downloaded from https://onlinelibrary.wiley.com/doi/10.1002/adfm.202205923 by CNR GROUP II Istituto di Scienza dell', Wiley Online Library on [23/05/2024]. See the Terms and Conditions (https://onlinelibrary.wiley.com/terms-and-conditions) on Wiley Online Library for rules of use; OA articles are governed by the applicable Creative Commons License

optimized Bridgman-Stockbarger method providing an unprecedented crystalline quality. Explicitly, the high crystalline quality of the GaTe samples was secured by the inspection of the X-ray diffraction (XRD) pattern (Figure S1, Supporting Information) and by the corresponding extraction of lattice parameters $a$ = 17.40 Å, $b$ = 10.46 Å, $c$ = 4.08 Å, $\gamma$ = 104.5° (ICSD, no.01-075-2220), consistent with previous results.[31] Moreover, the LEED pattern of the as-cleaved surfaces shows sharp spots (Figure 1c).

The ambient stability of defect-free and defective GaTe surfaces was assessed with NAP-XPS by exposing the sample to selective gases, i.e., $O_2$ and $H_2O$ (**Figure 4**). The core levels of as-cleaved GaTe surface displayed a single component, ascribed to GaTe, located at binding energy (BE) of ≈19 eV in Ga-3d$_{5/2}$ and 572.7 eV in Te-3d$_{5/2}$ (Figure 4a,b) (see also Ga-2p in Supporting Information, Figure S5 ). The stoichiometric GaTe sample is chemically inert toward $H_2O$ even after a $10^{11}$ L exposure (1 L = $10^{-6}$ Torr·s), as indicated by the analysis of Ga-3d (Figure 4a) and Te-3d (Figure 4b) core levels, congruently with the strongly unfavorable decomposition of $H_2O$ on defect-free GaTe (+127.36 kJ mol$^{-1}$). A weak component (≈10% of the spectral area) was revealed at ≈0.3–0.5 eV higher BE in both Ga-3d and Te-3d core levels with respect to the case of pristine GaTe, ascribable to the formation of an intermediate phase of $Ga_2Te_3$,[32] consistently with the evidence of an intermediate $Ga_2Se_3$ phase in the oxidation process of the parental compound GaSe.[33] Furthermore, our theoretical model indicates the energetic favorability of water intercalation, which could lead to a structural distortion, consistent with the experimental results (Figures S2 and S3, Supporting Information).

Similarly, no significant changes in stoichiometric GaTe were detected after a dose of $10^{11}$ L of $O_2$ on the sample. Indeed, the formation of surface oxides was not detected, in agreement with its predicted unfavourability, even though the decomposition of oxygen molecules is energetically feasible on defect-free GaTe. The only change in the core levels of Ga-3d and Te-3d after exposure to $O_2$ is the appearance of a new component due to $Ga_2Te_3$ (Figure 4a,b).

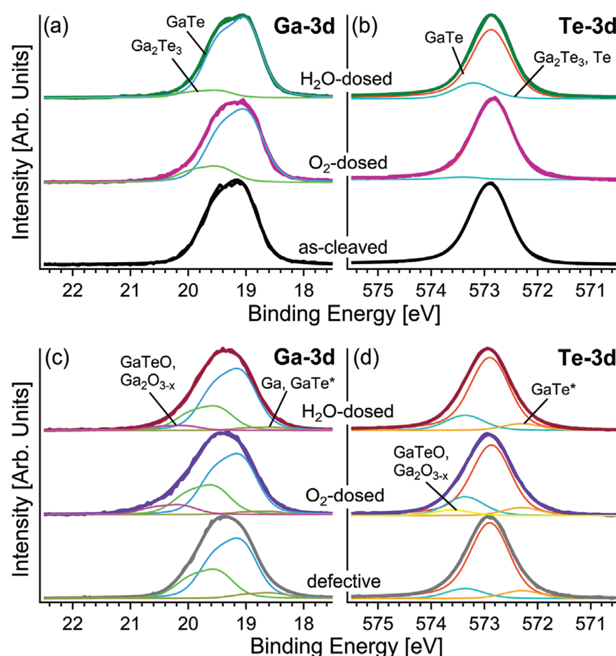


**Figure 4.** a) Ga-3d and b) Te-3d core levels for the as-cleaved surface of GaTe and its modification after dosing $10^{11}$ L $O_2$ and $H_2O$. Panels c,d) report the same for the defective $GaTe_{0.9}$ sample. The spectra were normalized to the maximum intensity. The photon energy was 1486.6 eV (Al K$_\alpha$).

To evaluate the influence of defects on the chemical reactivity of GaTe, Te vacancies were implanted by ion sputtering, so as to achieve different [Ga]:[Te] stoichiometries. In particular, $GaTe_{0.9}$ samples (Figure 4c,d) displayed broader core levels, due to the presence of further spectral components at lower and higher BE attributed to elemental Ga[34] and $Ga_2Te_3$ phase, respectively, as well as elemental Te.[35] In the defective $GaTe_{0.9}$ sample, the linewidth of core levels progressively broadened upon $O_2$ exposure, contrary to the case of the as-cleaved sample. The broadening is ascribed to the appearance of surface oxide phases, such as $Ga_2O_{3-x}$ and $GaTe_xO$ (≈10–15% of Ga-3d spectral area), and to the rise of the $Ga_2Te_3$ and Te(0) components. This finding is congruent with the favorable decomposition of molecular oxygen with further oxidation, predicted by our theoretical model in the presence of Te vacancies.

Concerning water reactivity, differently from the stoichiometric as-cleaved GaTe unmodified upon $H_2O$ exposure, in the water-dosed $GaTe_{0.9}$, a slight increase of the GaTeO/$Ga_2O_{3-x}$ component (≈5–7% of the total spectral area) in all core levels was observed (Figure 4c,d). It can be concluded that the effect of $H_2O$ is much lower than the effect of $O_2$ for both the defect-free and defective GaTe samples. We also investigated the water reactivity of partially oxidized surfaces, as extensively reported in Figures S6 and S7 (Supporting Information).

To assess chemical stability in the ambient atmosphere, core-level spectra (Ga-3d and Te-3d in **Figure 5**, with O-1s and valence band in Figure S8, Supporting Information) were

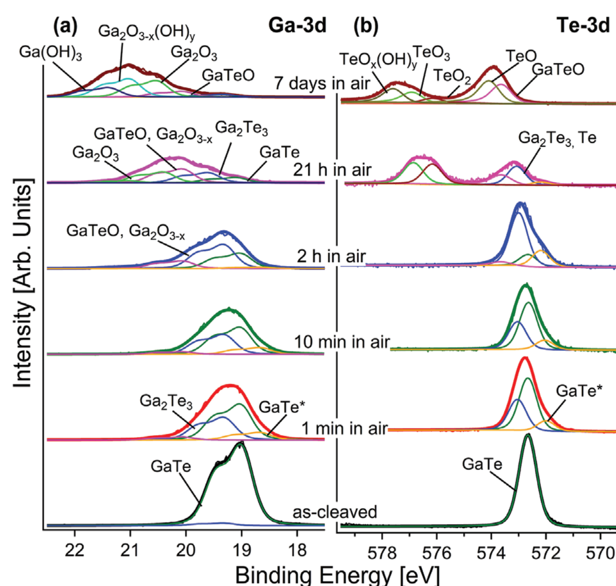


**Figure 5.** a) Ga-3d and b) Te-3d core levels for as-cleaved GaTe surface and its aging upon exposure to air for 1 min, 10 min, 2 h, 21 h, 7 days. The photon energy was 832 eV and the emission angle was 30° from the sample surface.


© 2022 The Authors. Advanced Functional Materials published by Wiley-VCH GmbH

measured after keeping both the defect-free and defective GaTe samples in air for a different amount of time. Actually, changes were evident already after 1 min, with the formation of components (GaTe*) at low BE associated with intercalation of ambient gases under the first layer and the concomitant decreased interaction with the underlying layer. At the same time, the $Ga_2Te_3$/Te(0) component is present at ≈0.3–0.5 eV higher BE in both Te-3d and Ga-3d with respect to the core levels of pristine GaTe. After 2 h in air, the GaTe surface exhibited a sub-monolayer gallium-oxide phase (with thickness <0.2 ML, with ML standing for monolayer), as well as an increased intensity for the $Ga_2Te_3$/Te(0) spectral component. According to theoretical results, the oxidation process starts at Te vacancies or from $Ga_2Te_3$ formed after the decomposition of water-intercalated GaTe (Figures S2 and S3, Supporting Information). After 21 h in air, the surface is passivated with an outermost oxide skin with GaTeO, $Ga_2O_3$,[36] $Ga_2O_3$, Te, and Te oxides ($TeO_x$, $TeO_2$, $TeO_3$)[37] (see TEM image in Figure 7f for direct imaging). These oxides further evolved to oxy-hydroxide species,[38] as a consequence of favorable water dissociation at defects on the oxidized surface.[39]

The assignment of each spectral component in XPS spectra is summarized in Table S1 (Supporting Information).

### 2.3. GaTe Nanosheets

Considering the potential beneficial effect of increasing the surface-to-volume ratio in nanosheets compared to the bulk crystals for applications in catalysis and gas sensing, we assessed the stability of exfoliated GaTe nanosheets by synchrotron-based XPEEM, which enables the acquisition of XPS spectra with nanoscale spatial resolution. GaTe nanosheets can be easily noticed as dark areas in the substrate Si-2p signal in the XPEEM image in **Figure 6**a. The flakes appear bright in the Te-4d (Figure 6b) and Ga-3d XPEEM images. The analysis of μ-XPS spectra, collected with low-energy photons to improve surface sensitivity, indicated that GaTe nanosheets are mostly oxidized, with gallium-oxide components dominating the Ga-3d spectra. Our results are also consistent with the reduction of the photoluminescence by $10^4$–$10^5$ for GaTe thickness reduced to 10 nm,[40] previously ascribed to non-radiative carrier escape via surface states.[40]

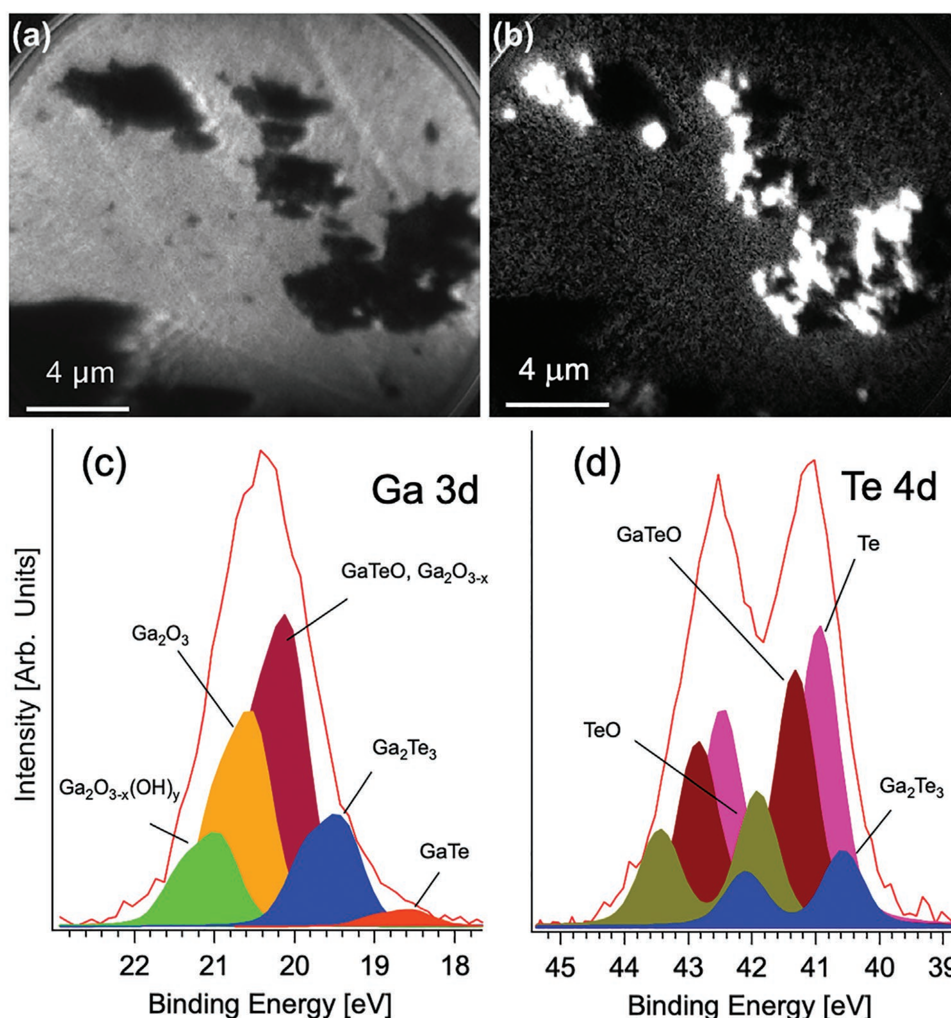


**Figure 6.** XPEEM images at the a) Si-2p, b) Te-4d core levels. XPS spectra in the region of c) Ga-3d and d) Te-4d core levels. Photon energy was 150 eV.


© 2022 The Authors. Advanced Functional Materials published by Wiley-VCH GmbH

16163028, 2022, 41, Downloaded from https://onlinelibrary.wiley.com/doi/10.1002/adfm.202205923 by CNR GROUP II Istituto di Scienza dell', Wiley Online Library on [23/05/2024]. See the Terms and Conditions (https://onlinelibrary.wiley.com/terms-and-conditions) on Wiley Online Library for rules of use; OA articles are governed by the applicable Creative Commons License

16163028, 2022, 41, Downloaded from https://onlinelibrary.wiley.com/doi/10.1002/adfm.202205923 by CNR GROUP II Istituto di Scienza dell', Wiley Online Library on [23/05/2024]. See the Terms and Conditions (https://onlinelibrary.wiley.com/terms-and-conditions) on Wiley Online Library for rules of use; OA articles are governed by the applicable Creative Commons License

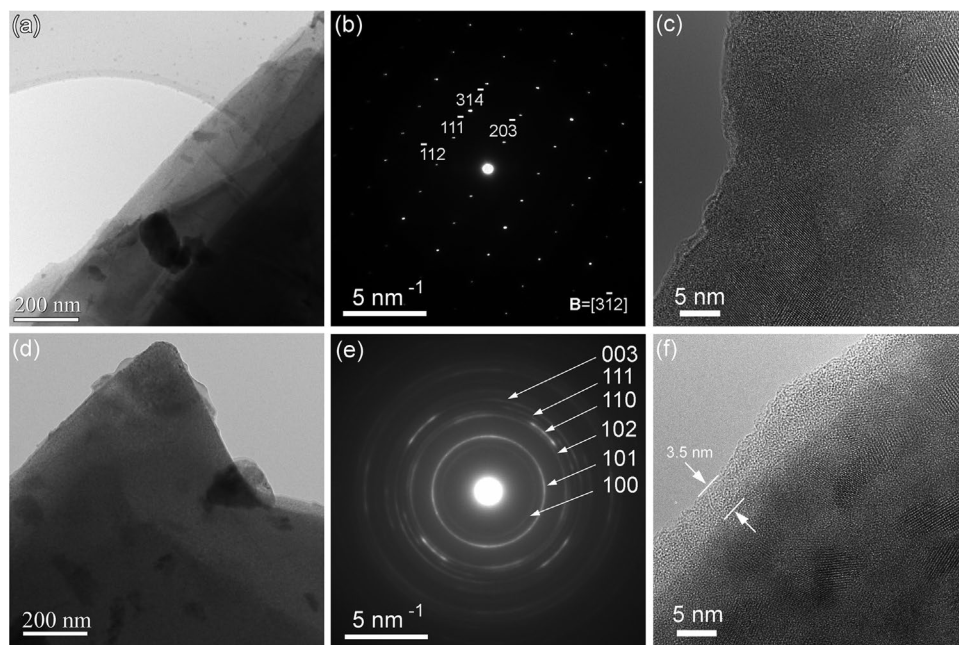


**Figure 7.** Low-magnification TEM image of GaTe nanosheets a) soon after preparation and d) after 3 months in air, with their associated SAED pattern in panels (b) and (e). Correspondingly, panels represent HRTEM images at the border of one GaTe nanosheet c) soon after preparation and f) after 3 months in air, with the latter showing the presence of an enveloping amorphous oxide layer with a thickness of ≈3.5 nm.

Moreover, the presence of Te(0) species in nanosheets was evident from the analysis of Te-3d core level.

Further information on the microstructure of nanosheets was obtained by TEM. The selected area electron diffraction (SAED) pattern in **Figure 7**b corresponds to an area selected from the nanosheet imaged in Figure 7a, revealing the $B = [3{-}12]_{GaTe}$ zone axis orientation of monoclinic GaTe.

It is worth reminding that previous reports indicated the occurrence of a phase transition from monoclinic to hexagonal structure for ultrathin GaTe platelets.[41] We do not observe any phase transition, even for the lowest thickness of GaTe nanosheets.

In addition, the same specimen was re-analyzed after three months in air (Figure 7d–f). The corresponding SAED pattern (Figure 7e), recorded from a large area of the aged nanosheet, revealed a polycrystalline structure. The continuous and diffuse aspect of the diffraction rings indicated a nanometric size of the crystalline domains. The diffraction rings were broken into circular segments, illustrating a certain nanotexture. The crystal structure identified by measuring the SAED pattern corresponds to metallic tellurium (cif file no. 1011098). All diffraction rings in the SAED pattern were thus assigned to the triclinic structure of metallic tellurium, as indicated by the Miller indices in Figure 7e. In aged GaTe nanosheets, one could not identify diffraction spots related to the GaTe crystal structure, in excellent agreement with μ-XPS results in Figure 6c-d and with energy dispersive X-ray spectrometry (EDS) spectra (Figure S10, Supporting Information).

Accordingly, one can conclude that the formed gallium-oxide skin is amorphous, as inferred by the absence of $Ga_2O_3$ diffraction rings in the SAED patterns. This conclusion is supported by the high-resolution TEM (HR-TEM) micrograph in Figure 7e recorded in the proximity of the nanosheet border. Definitely, the nanosheet was enveloped by an amorphous shell with a thickness of ≈3.5 nm, while its central part consisted of a mixture of crystalline Te nanograins and amorphous material. Similar results were obtained on the TEM specimen freshly prepared from the same liquid suspension after 3 months.

### 2.4. Photo(Electro)Catalysis: Effects of Thickness and Surface Oxidation

Considering the presence of the amorphous $Ga_2O_3$ skin on the surface of GaTe (both bulk and nanosheets), we evaluated the catalytic activity of GaTe-based systems. The calculated free energy diagram of HER in acidic media (**Figure 8**a) indicates that pristine defect-free bulk GaTe is unsuitable for HER due to an energy cost of 0.2 eV per $H^+$, which even increases in the

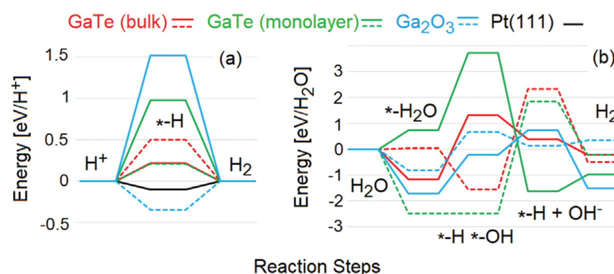


**Figure 8.** Calculated free energy diagrams for HER in acidic a) and alkali b) media over discussed substrates with (dashed lines) and without (solid lines) anionic defects/vacancies. Data for Pt(111) are reported for the sake of comparison. The notation *-R corresponds to adsorption on the substrate.

 © 2022 The Authors. Advanced Functional Materials published by Wiley-VCH GmbH

monolayer regime up to 1.0 eV per $H^+$. On the other hand, the defective $GaTe_{0.97}$ is competitive with state-of-the-art catalysts Pt (−0.3 vs −0.1 eV per $H^+$). Considering the reduction of cost of raw materials by 160 times compared to Pt-based electrocatalysts,[42] we can propose the self-assembled $Ga_2O_3$/GaTe heterostructure as a catalyst for HER in acidic media.

In the case of alkali media, the decomposition of water can be discussed as a two-step process with a rather high energy cost (more than 2.5 eV/OH) in the second step, corresponding with the formation of the free $OH^-$ group. Another approach could be a multistep process. In this case, the water molecule first adsorbs on the surface (*-$H_2O$), with a successive decomposition (*-H *-OH) with further gradual desorption of $OH^-$ (*-H + $OH^-$ step) and, finally, molecular hydrogen is formed by Tafel step (2*-H → $H_2$). Since the magnitude of endothermic steps of HER over $Ga_2O_{3-x}$ is manifestly smaller (>0.5 eV) than over $GaTe_x$ substrates (see Figure 8b), the $Ga_2O_{3-x}$ skin could be proposed as the chemically active part of GaTe-based photocatalytic devices.

Moreover, GaTe has recently been proposed as a photocatalyst.[15,43] Accordingly, the critical assessment of the electronic structure of $Ga_2O_3$/GaTe interface is essential. For this purpose, we calculated the electronic structure of a $Ga_2O_3$ slab and non-oxidized GaTe bilayer, with and without anionic vacancies. Results of the calculations (Figure S9, Supporting Information) demonstrated that the valence-band maximum (VBM) and conduction-band minimum (CBM) of both GaTe and $GaTe_{0.97}$ display energies ≈2 eV above the CBM of $Ga_2O_x$. Based on the calculated electronic structure, we can discuss photocatalysis on $Ga_2O_3$/GaTe interface as a two-step process. In the first step, a photo-induced transition of electrons occurs from valence to conduction bands of the $GaTe_x$ substrate. In the second step, photo-generated electrons migrate from conduction bands of the $GaTe_x$ substrate to the states with lower energies in the conduction band of the $Ga_2O_x$ skin, where these electrons will participate in electrochemical reactions on chemically active sites on the surface (see Figure 8).

Note that, due to valuable amount of defects, valence band (VB) and conduction band (CB) of pristine and defective GaTe (GaTe and $GaTe_x$) correspond to defect states of the CB of the $Ga_2O_{3-x}$ skin (narrow peaks in electronic structure in Figure S9 in the Supporting Information). As VBM and CBM of both parts of the interface are formed by defects states, all transitions between these bands can be considered as direct (**Figure 9**). The proposed model of photo- and chemical activity of $Ga_2O_3$/GaTe interface can explain the efficient photoelectrocatalytic properties for water splitting previously observed for GaTe.[16,43a]

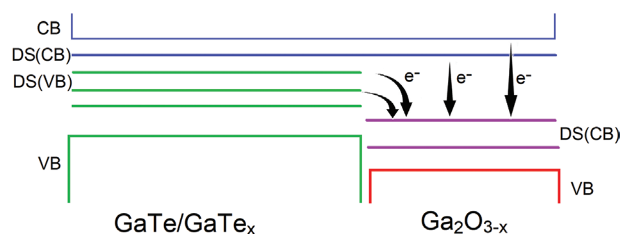


**Figure 9.** A sketch of non-radiative electronic transition from defect states (DS) of VB and CB of GaTe/$GaTe_x$ to defect states of CB of $Ga_2O_{3-x}$.

Thus, based on theoretical modeling, one can propose the $Ga_2O_{3-x}$/$GaTe_x$ interface as a promising heterostructure for electrocatalytic reactions, combining the high photoabsorption of the $GaTe_x$ with the stability and catalytic efficacy of the transparent surface oxide layer.

Previously, GaTe-based heterostructures were only studied for the case of GaTe/ZnO, being a suitable platform for efficient photocatalytic water splitting[16] and for solar cells (power conversion efficiency of 6.64%[44]).

### 2.5. Gas Sensing with Pristine GaTe and $Ga_2O_3$/GaTe Heterostructure

Finally, we assessed the effect of surface oxidation on the sensing properties of GaTe-based systems. For this purpose, we simulated the adsorption of water, ammonia, and nitrogen dioxide on i) pristine GaTe; ii) oxygenated GaTe ($GaTeO_x$); iii) a $Ga_2O_3$ slab; and sub-stoichiometric gallium-oxide, exhibiting oxygen vacancies in the surface layer ($Ga_2O_{2.97}$). Considering that $Ga_2O_3$-based gas sensors operate at temperatures as high as 600–650 °C,[45] we performed additional calculations of the free energy of the physical adsorption at 600 °C.

To model the oxidized surface of GaTe, we used the structure shown in Figure 3c after doubling the amount of oxygen in the surface layer. The results of calculations, summarized in **Table 2**, demonstrate that the cavities of the surface layer created by the peculiar structure of GaTe (Figures 1a and 3a) represent perfect spots for the stable adsorption of all considered species.

Large magnitudes of negative Gibbs free energy (Table 2) correspond to the formation of robust non-covalent bonds between substrate and analytes, associated with charge transfer.

Despite a large amount of transferred charge (above 0.3 e–, Table 2), the adsorption of considered analytes influenced the charge density only in close vicinity of the adsorption site,

**Table 2.** Differential Gibbs free energy of physisorption at room temperature and at T = 600 °C (kJ $mol^{-1}$) and amount of charge transfer (in electrons) for adsorption of $H_2O$, $NH_3$, and $NO_2$ on pristine and oxidized surface of bulk GaTe and gallium oxide with ($Ga_2O_{2.97}$) and without ($Ga_2O_3$) oxygen vacancies in the surface layer.

| Analyte | Substrate | $\Delta G$ [kJ $mol^{-1}$] $T$ = 25 °C | $\Delta G$ [kJ $mol^{-1}$] $T$ = 600 °C | $\Delta e^-$ |
|---|---|---|---|---|
| $H_2O$ | GaTe | −92.5 | −82.3 | −0.57 |
| | $GaTeO_x$ | −239.2 | −221.0 | −0.60 |
| | $Ga_2O_3$ | −145.7 | −126.5 | −0.48 |
| | $Ga_2O_{2.97}$ | −58.1 | −37.9 | −0.36 |
| $NH_3$ | GaTe | −115.6 | −103.1 | +0.42 |
| | $GaTeO_x$ | −341.4 | −329.9 | +0.78 |
| | $Ga_2O_3$ | −154.7 | −142.2 | +0.44 |
| | $Ga_2O_{2.97}$ | −77.8 | −65.3 | +0.36 |
| $NO_2$ | GaTe | −181.6 | −161.5 | −0.74 |
| | $GaTeO_x$ | −198.5 | −177.4 | −0.77 |
| | $Ga_2O_3$ | −11.5 | +7.4 | −0.30 |
| | $Ga_2O_{2.97}$ | −35.6 | −15.5 | −0.35 |


© 2022 The Authors. Advanced Functional Materials published by Wiley-VCH GmbH

16163028, 2022, 41, Downloaded from https://onlinelibrary.wiley.com/doi/10.1002/adfm.202205923 by CNR GROUP II Istituto di Scienza dell', Wiley Online Library on [23/05/2024]. See the Terms and Conditions (https://onlinelibrary.wiley.com/terms-and-conditions) on Wiley Online Library for rules of use; OA articles are governed by the applicable Creative Commons License

16163028, 2022, 41, Downloaded from https://onlinelibrary.wiley.com/doi/10.1002/adfm.202205923 by CNR GROUP II Istituto di Scienza dell, Wiley Online Library on [23/05/2024]. See the Terms and Conditions (https://onlinelibrary.wiley.com/terms-and-conditions) on Wiley Online Library for rules of use; OA articles are governed by the applicable Creative Commons License

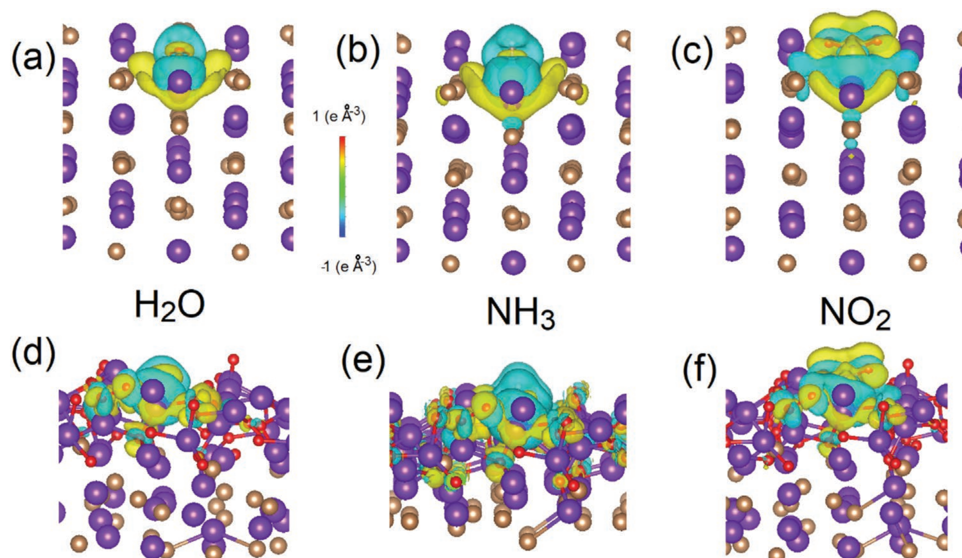


**Figure 10.** The change of charge density after adsorption of a,d) $H_2O$, b,e) $NH_3$, and c,f) $NO_2$ on a–c) pristine and d–f) oxidized surfaces of bulk GaTe.

without affecting underlying layers (**Figure 10**a–c). This localization of the charge redistribution limits the sensing capabilities of pure GaTe. In addition, the extreme chemical instability of GaTe with inevitable surface oxidation even at room temperature (discussed in previous sections) makes impossible its usage in gas-sensing devices. On the other hand, the oxidation of the GaTe surface provides a significant increase in the magnitudes of i) the differential Gibbs free energy of physisorption and ii) transferred charges (Table 2), due to the structural disorder of surface and subsurface oxide layers, already in the early stages of surface oxidation (namely, $GaTeO_x$). The changes in the charge densities caused by physisorption of analytes broadly distributed in surface and even subsurface layers (Figure 10d–f) affect electrical properties of subsurface area. The ultimate formation of the $Ga_2O_x$ skin leads to quantitative changes in the values of the adsorption energies and transferred charge without noticeable differences compared to the case of the oxygenated GaTe surface ($GaTeO_x$). Thus, based on the theoretical model, we can propose that surface oxidation of GaTe induces an increase in the area of charge redistribution after adsorption. Considering that both GaTe and $GaTeO_x$ are chemically instable with an ultimate evolution into $Ga_2O_3$, we propose the $Ga_2O_3$/GaTe interface as a perspective material for gas sensing, with an operational temperature, which could be extended up to 600 °C. This is relevant for the identification and quantification of chemical species in several industrial applications (such as combustion processes[46]), involving high temperatures and chemical contaminants (Refs. [46,47] for a review). Thus, $Ga_2O_3$/GaTe-based gas sensors provide thermal and long-term stability, sensitivity, reproducibility, and selectivity.

## 3. Conclusions

The fast degradation of GaTe vdW semiconductor in the ambient atmosphere is commonly assumed as disadvantageous for applications in photonics and optoelectronics. However, findings here reported open new perspectives for GaTe-based applications, in consideration of the capabilities enabled by surface oxidation, driven by the inevitable presence of Te vacancies. Definitely, our modeling, complemented by surface-science experiments, shows a promising prospect associated with the presence of Te vacancy defects in all applications of GaTe, based on surface chemical reactions.

While defect-free GaTe monolayer is chemically stable, the presence of defects and edges makes the monolayer unstable against water and oxygen decomposition on the vacancies. Similarly, bulk GaTe is unstable in air, with the subsequent inevitable formation of $Ga_2O_3$ skin. Thus, a protective wide-energy-gap $Ga_2O_3$ skin is naturally and inevitably formed over narrow-energy-gap GaTe. Such a vertical heterostructure is responsible for the pronounced light harvesting and sensing properties of GaTe.

While the instability of bulk pristine GaTe in water makes it not a suitable candidate for electro- and photocatalysis, the unavoidable surface oxidation of GaTe into $Ga_2O_3$ produces a self-assembled $Ga_2O_3$/GaTe heterostructure, which is unexpectedly more effective than pristine GaTe in electrocatalysis, photocatalysis, and gas sensing.

Remarkably, while HER for pristine GaTe shows an energy barrier of 0.2 and 0.5 eV/$H^+$ for bulk and monolayer, the Heyrovsky step ($H_{ads}$ + $H^+$ + $e^-$ $\rightarrow$ $H_2$) of HER is energetically favorable in sub-stoichiometric $Ga_2O_{2.97}$ (–0.3 eV per $H^+$).

Moreover, the wide-band-gap oxide skin formed over narrow-band-gap $GaTe_x$ upon air exposure makes the self-assembled gallium-oxide/gallium-telluride heterostructure suitable for light harvesting.

Finally, calculations show that the sensing properties of GaTe are enhanced by surface oxidation, which induces an increase in the area of charge redistribution after adsorption of analytes, such as $H_2O$, $NH_3$, and $NO_2$. Remarkably, $Ga_2O_3$/GaTe enables high-temperature gas sensing at operational temperatures as high as 600 °C, so as to enable its use for detection of gaseous species in combustion processes.


© 2022 The Authors. Advanced Functional Materials published by Wiley-VCH GmbH

These findings pave the way for a novel generation of efficient and cheap (photo-) electrocatalysts and gas sensors, based on self-assembled heterostructures produced by exploiting the natural interaction with the ambient atmosphere.

## 4. Experimental Section

*Theory*: The atomic structure, energetics of chemical modification, and sensing properties were modeled by DFT-based methods implemented in the QUANTUM-ESPRESSO pseudopotential code.[48] considering the GGA–PBE + van der vdW approximation.[49] This computational framework was feasible for the description of the interactions between molecules and surfaces.[50] The energy cutoffs were 25 and 400 Ry for the plane-wave expansion of the wave functions and the charge density, respectively. The 3 ×6 × 2 Monkhorst-Pack *k*-point grid for the Brillouin sampling was adopted for all considered systems.[51] For the modeling of the GaTe surface, a slab of two layers of 2 × 4 × 2 supercell of GaTe was used.

A monoclinic atomic bilayer structure with the bulk lattice parameters was used for the modeling of the chemical, physical properties, and electronic structure of bulk and monolayer GaTe. The separation between layers within periodic boundary conditions was > 60 Å, thus excluding any possible contribution from the interactions between the slabs. For the modeling of the surface of GaTe bulk crystal, calculations with the optimization of the only atomic positions were performed. Contrary, in the case of the modeling of monolayer GaTe, both atomic positions and lattice parameters were optimized. Hence the model of monolayer GaTe considered contributions from additional degrees of freedom of free-standing membranes. It was worth mentioning that the contributions related to the expansion or contraction of monolayer were essential for a correct evaluation of the chemical stability of metal monochalcogenides, as demonstrated previously for the cases of InSe and GaSe nanosheets.[50]

For the evaluation of the energy required for the formation of Te vacancies, the extraction of a single Te atom from a supercell in bulk tellurium was modeled. In the case of bilayer GaTe, one Te atom was removed from the surface layer. The values of the enthalpies of physisorption were calculated by the following formula:

$$\Delta H_{\mathrm{phys}} = [E_{\mathrm{host+mol}} - (E_{\mathrm{host}} + E_{\mathrm{guest}})] \tag{4}$$

where $E_{\mathrm{host}}$ is the total energy of a pristine surface and $E_{\mathrm{guest}}$ is the total energy of the single molecules of selected species in an empty box. Note that, for all adsorbates, only the gaseous phase at low concentration was considered, thus interactions between molecules of analytes in the gaseous phase did not include in $E_{\mathrm{guest}}$. The energy of chemical adsorption was defined as the difference between the total energy of the system with a physisorbed molecule and the total energy of the same system after the decomposition of the same molecule on the surface. For the case of physisorption, differential Gibbs free energy was also estimated by the following formula:

$$\Delta G = \Delta H - T\Delta S \tag{5}$$

where $T$ is the temperature and $\Delta S$ is the change of entropy of adsorbed molecule, which was estimated considering the gas→liquid transition by the standard formula:

$$\Delta S = \frac{\Delta H_{\mathrm{vaporization}}}{T} \tag{6}$$

where $\Delta H_{\mathrm{vaporization}}$ is the measured differential enthalpy of vaporization.

*Single-Crystal Growth*: High-quality GaTe single crystals are grown by the Bridgman-Stockbarger method. Crystal growth was performed in a furnace with two different temperature zone. The temperature program for GaTe is given in Figure S1 (Supporting Information). Samples were cleaved by adhesive tape.

*X-Ray Photoemission Spectroscopy*: Photoelectron spectroscopy measurements were performed at room temperature, in two different experimental apparatuses, both equipped with Scienta R3000 hemispherical electron analyzers. NAP- XPS measurements were performed using Al $K_\alpha$ at the Charles University in Prague, while soft-X ray synchrotron radiation XPS was performed in ultra-high vacuum conditions (base pressure < $10^{-10}$ mbar) at the BACH beamline at Elettra synchrotron, Trieste, Italy. These two different XPS facilities were used to achieve complementary information. Synchrotron-based XPS enables high resolution, fast data acquisition and tunable photon energy, while NAP-XPS allows the measurements directly in a high-pressure chamber (1 mbar $O_2$ and $H_2O$ vapor), where the sample is kept in conditions close to the ambient environment during data acquisition.

Ga-3d, Te-3d (and O-1s) were fitted with by a superposition of Voigt doublet components after subtracting a Shirley background.

The as-cleaved samples were completely free from contaminants, including carbon and oxygen, as confirmed by the survey spectrum (Figure S4, Supporting Information).

*Liquid-Phase Exfoliation of Nanosheets*: GaTe crystals were ground in a mortar to obtain a fine powder. After grinding, 10 mg of powderized GaTe were dispersed in 20 mL of isopropyl alcohol (IPA, ACS Reagent, ≥99.8%, Sigma-Aldrich), and sonicated for 3 h in a bath sonicator in a thermostat bath to avoid temperature rise (T ≤ 22 °C). Subsequently, with centrifugation at 5000 rpm a make-up of IPA solvent was carried out to discard the waste IPA. Last centrifugation at 1000 rpm was achieved to separate the exfoliated flakes from unexfoliated counterparts. Finally, the supernatant was collected for characterization.

*Spectroscopic Photoemission and Low-Energy Electron Microscopy*: XPEEM measurements were carried out on the liquid-phase exfoliated nanosheets at the Nanospectroscopy beamline of the Elettra synchrotron (Trieste, Italy). GaTe nanosheets were deposited by drop casting from dispersions in a liquid suspension onto an Au film-covered silicon substrate. The Nanospectroscopy end-station is equipped with a Spectroscopic PhotoEmission and Low-Energy Electron Microscope (SPELEEM). The soft X-ray beam was focused to illuminate the small field of view (2 to 30 microns), and the emitted photoelectrons were imaged by electron optics onto an area detector. The lateral resolution in XPEEM mode was ≈30 nm with energy resolution in spectroscopic imaging of <0.2 eV. Using electrons generated by the $LaB_6$ electron source in the microscope, microspot LEED patterns were obtained using the instrument in the diffraction mode by imaging the backfocal plane of the objective lens.

*Transmission Electron Microscope*: TEM investigations were performed with a JEM ARM 200F instrument operated at 200 kV (0.19 nm point resolution). The TEM specimens were prepared by drop-casting a droplet from GaTe nanosheets dispersed in a liquid suspension onto copper grids provided with a lacey carbon membrane.

## Supporting Information

Supporting Information is available from the Wiley Online Library or from the author.

## Acknowledgements

CG and MCI acknowledge funding through the contract POC 332/390008/29.12.2020-SMIS 109522 AP thanks CERIC-ERIC for granting access to the facilities in Trieste, Prague, and Magurele. FB and SN acknowledge support from MUR (EuroFEL project).

Open Access Funding provided by Universita degli Studi dell'Aquila within the CRUI-CARE Agreement.

## Conflict of Interest

The authors declare no conflict of interest.



© 2022 The Authors. Advanced Functional Materials published by Wiley-VCH GmbH

16163028, 2022, 41, Downloaded from https://onlinelibrary.wiley.com/doi/10.1002/adfm.202205923 by CNR GROUP II Istituto di Scienza dell', Wiley Online Library on [23/05/2024]. See the Terms and Conditions (https://onlinelibrary.wiley.com/terms-and-conditions) on Wiley Online Library for rules of use; OA articles are governed by the applicable Creative Commons License

## Authors Contribution

The project has been conceived and coordinated by AP. FB and SN carried out synchrotron-based XPS. MV carried out NAP-XPS. TOM and AL carried out nanospectroscopy experiments. All XPS data were analyzed by FB, SN, and GDO. TEM experiments were performed by CG and MCI. FM carried out ARPES experiments, with the support of MJ. Single crystals were grown by BG, SD, and AP. Liquid-phase exfoliation of bulk crystals was carried out by GDO and SS. The theoretical model was done by DWB. Figures were prepared by GDO, FB, SN, DWB, CG, and SS. The manuscript was written by SD, DWB, GDO, and AP.

## Data Availability Statement

The data that support the findings of this study are available from the corresponding author upon reasonable request.

## Keywords

gallium telluride, hydrogen evolution reaction, DFT calculations, nanospectroscopy, surface science

Received: May 24, 2022
Revised: June 23, 2022
Published online: August 7, 2022

[1] a) L. Maduro, M. Noordam, M. Bolhuis, L. Kuipers, S. Conesa-Boj, *Adv. Funct. Mater.* **2022**, *32*, 2107880; b) V. K. Sangwan, S. V. Rangnekar, J. Kang, J. Shen, H. S. Lee, D. Lam, J. Shen, X. Liu, A. C. M. de Moraes, L. Kuo, J. Gu, H. Wang, M. C. Hersam, *Adv. Funct. Mater.* **2021**, *31*, 2107385; c) W. Zhu, C. Song, L. Han, H. Bai, Q. Wang, S. Yin, L. Huang, T. Chen, F. Pan, *Adv. Funct. Mater.* **2022**, *32*, 2108953.
[2] a) J. Luo, L. Xu, H. Liu, Y. Wang, Q. Wang, Y. Shao, M. Wang, D. Yang, S. Li, L. Zhang, Z. Xia, T. Cheng, Y. Shao, *Adv. Funct. Mater.* **2022**, *32*, 2112151; b) A. K. Geim, *Rev. Mod. Phys.* **2011**, *83*, 851; c) K. S. Novoselov, *Rev. Mod. Phys.* **2011**, *83*, 837; d) M. S. Vitiello, *J. Phys.: Mater.* **2019**, *3*, 014008; e) A. Di Gaspare, E. A. A. Pogna, L. Salemi, O. Balci, A. R. Cadore, S. M. Shinde, L. Li, C. di Franco, A. G. Davies, E. H. Linfield, A. C. Ferrari, G. Scamarcio, M. S. Vitiello, *Adv. Funct. Mater.* **2021**, *31*, 2008039.
[3] K. Novoselov, *Nat. Mater.* **2007**, *6*, 720.
[4] D. Li, L. Zhao, Q. Xia, J. Wang, X. Liu, H. Xu, S. Chou, *Adv. Funct. Mater.* **2022**, *32*, 2108153.
[5] D. Xu, L. Chen, X. Su, H. Jiang, C. Lian, H. Liu, L. Chen, Y. Hu, H. Jiang, C. Li, *Adv. Funct. Mater.* **2022**, *32*, 2110223.
[6] D. Ouyang, X. Tong, S. Liu, J. Wang, Y. Zhao, R. Liu, X. Zhao, N. Zhang, F. Cao, Y. Liu, Y. Li, L. Li, T. Zhai, *Adv. Funct. Mater.* **2022**, *32*, 2113052.
[7] D. S. Gavhane, A. D. Sontakke, M. A. van Huis, *Adv. Funct. Mater.* **2022**, *32*, 2106450.
[8] C. H. Lee, Y. Park, S. Youn, M. J. Yeom, H. S. Kum, J. Chang, J. Heo, G. Yoo, *Adv. Funct. Mater.* **2022**, *32*, 2107992.
[9] L. Gouskov, A. Gouskov, *Phys. Status Solidi A* **1979**, *51*, K213.
[10] P. Hu, J. Zhang, M. Yoon, X.-F. Qiao, X. Zhang, W. Feng, P. Tan, W. Zheng, J. Liu, X. Wang, J. C. Idrobo, D. B. Geohegan, K. Xiao, *Nano Res.* **2014**, *7*, 694.
[11] S. Huang, Y. Tatsumi, X. Ling, H. Guo, Z. Wang, G. Watson, A. A. Puretzky, D. B. Geohegan, J. Kong, J. Li, T. Yang, R. Saito, M. S. Dresselhaus, *ACS Nano* **2016**, *10*, 8964.
[12] J. Camassel, P. Merle, H. Mathieu, A. Gouskov, *Phys. Rev. B* **1979**, *19*, 1060.
[13] J. Susoma, L. Karvonen, A. Säynätjoki, S. Mehravar, R. A. Norwood, N. Peyghambarian, K. Kieu, H. Lipsanen, J. Riikonen, *Appl. Phys. Lett.* **2016**, *108*, 073103.
[14] F. Liu, H. Shimotani, H. Shang, T. Kanagasekaran, V. Zolyomi, N. Drummond, V. I. Fal'ko, K. Tanigaki, *ACS Nano* **2014**, *8*, 752.
[15] L.-C. Tien, Y.-C. Shih, *Nanomaterials* **2021**, *11*, 778.
[16] Q. Li, X. Ma, H. Liu, Z. Chen, H. Chen, S. Chu, *ACS Appl. Mater. Interfaces* **2017**, *9*, 18836.
[17] a) Z. Wang, M. Safdar, M. Mirza, K. Xu, Q. Wang, Y. Huang, F. Wang, X. Zhan, J. He, *Nanoscale* **2015**, *7*, 7252; b) G. Yu, Z. Liu, X. Xie, X. Ouyang, G. Shen, *J. Mater. Chem. C* **2014**, *2*, 6104.
[18] S. S. Abed Al- Abbas, M. K. Muhsin, H. R. Jappor, *Chem. Phys. Lett.* **2018**, *713*, 46.
[19] a) N. Kolesnikov, E. Borisenko, D. Borisenko, A. Timonina, *J. Cryst. Growth* **2013**, *365*, 59; b) A. Kunjomana, M. Teena, K. Chandrasekharan, *J. Appl. Crystallogr.* **2014**, *47*, 1841.
[20] a) J. J. Fonseca, S. Tongay, M. Topsakal, A. R. Chew, A. J. Lin, C. Ko, A. V. Luce, A. Salleo, J. Wu, O. D. Dubon, *Adv. Mater.* **2016**, *28*, 6465; b) S. Yang, H. Cai, B. Chen, C. Ko, V. O. Ozcelik, D. F. Ogletree, C. E. White, Y. Shen, S. Tongay, *Nanoscale* **2017**, *9*, 12288; c) M. Kotha, T. Murray, D. Tuschel, S. Gallis, *Nanomaterials* **2019**, *9*, 1510; d) A. R. Chew, J. J. Fonseca, O. D. Dubon, A. Salleo, *Adv. Funct. Mater.* **2017**, *27*, 1605038.
[21] E. Mercado, Y. Zhou, Y. Xie, Q. Zhao, H. Cai, B. Chen, W. Jie, S. Tongay, T. Wang, M. Kuball, *ACS Omega* **2019**, *4*, 18002.
[22] J. Susoma, J. Lahtinen, M. Kim, J. Riikonen, H. Lipsanen, *AIP Adv.* **2017**, *7*, 015014.
[23] H. Wang, M.-L. Chen, M. Zhu, Y. Wang, B. Dong, X. Sun, X. Zhang, S. Cao, X. Li, J. Huang, L. Zhang, W. Liu, D. Sun, Y. Ye, K. Song, J. Wang, Y. Han, T. Yang, H. Guo, C. Qin, L. Xiao, J. Zhang, J. Chen, Z. Han, Z. Zhang, *Nat. Commun.* **2019**, *10*, 2302.
[24] M. Kotha, T. Murray, D. Tuschel, S. Gallis, *Nanomaterials* **2019**, *9*, 1510.
[25] S. Yang, Y. Qin, B. Chen, V. O. Özçelik, C. E. White, Y. Shen, S. Yang, S. Tongay, *ACS Appl. Mater. Interfaces* **2017**, *9*, 44625.
[26] H. Cai, B. Chen, G. Wang, E. Soignard, A. Khosravi, M. Manca, X. Marie, S. L. Chang, B. Urbaszek, S. Tongay, *Adv. Mater.* **2017**, *29*, 1605551.
[27] C. Rocha Leão, V. Lordi, *Phys. Rev. B* **2011**, *84*, 165206.
[28] Z. Wang, K. Xu, Y. Li, X. Zhan, M. Safdar, Q. Wang, F. Wang, J. He, *ACS Nano* **2014**, *8*, 4859.
[29] a) P. Galiy, T. Nenchuk, A. Ciszewski, P. Mazur, S. Zuber, I. Yarovets, *Metallofiz. Noveishie Tekhnol* **2015**, *37*, 789; b) O. A. Balitskii, B. Jaeckel, W. Jaegermann, *Phys. Lett. A* **2008**, *372*, 3303.
[30] a) L. C. Muhimmah, C.-H. Ho, *Appl. Surf. Sci.* **2021**, *542*, 148593; b) N. N. Kolesnikov, E. B. Borisenko, D. N. Borisenko, A. V. Timonina, *J. Cryst. Growth* **2013**, *365*, 59.
[31] Q. Zhao, T. Wang, Y. Miao, F. Ma, Y. Xie, X. Ma, Y. Gu, J. Li, J. He, B. Chen, *Phys. Chem. Chem. Phys.* **2016**, *18*, 18719.
[32] O. Balitskii, V. Savchyn, *Mater. Sci. Semicond. Process.* **2007**, *10*, 124.
[33] J. Liu, J. Liv, L. Gu, H. Wu, G. Han, D. Wang, J. Zhou, X. Gong, D. Yang, S. Zheng, *Appl. Surf. Sci.* **2022**, 152774.
[34] R. Wasielewski, M. Grodzicki, J. Sito, K. Lament, P. Mazur, A. Ciszewski, *Acta Phys. Pol. A* **2017**, *132*, 354.
[35] M. O. Reese, C. L. Perkins, J. M. Burst, S. Farrell, T. M. Barnes, S. W. Johnston, D. Kuciauskas, T. A. Gessert, W. K. Metzger, *J. Appl. Phys.* **2015**, *118*, 155305.
[36] a) S. Ghose, S. Rahman, L. Hong, J. S. Rojas-Ramirez, H. Jin, K. Park, R. Klie, R. Droopad, *J. Appl. Phys.* **2017**, *122*, 095302; b) C. Kura, Y. Aoki, E. Tsuji, H. Habazaki, M. Martin, *RSC Adv.* **2016**, *6*, 8964.
[37] T. Wei, J. Wei, K. Zhang, L. Zhang, *Phot. Res.* **2017**, *5*, 22.
[38] L.-Y. Zhang, K.-H. Lii, *Dalton Trans.* **2019**, *48*, 15231.


© 2022 The Authors. Advanced Functional Materials published by Wiley-VCH GmbH

16163028, 2022, 41, Downloaded from https://onlinelibrary.wiley.com/doi/10.1002/adfm.202205923 by CNR GROUP II Istituto di Scienza dell', Wiley Online Library on [23/05/2024]. See the Terms and Conditions (https://onlinelibrary.wiley.com/terms-and-conditions) on Wiley Online Library for rules of use; OA articles are governed by the applicable Creative Commons License

[39] J. Fester, M. García-Melchor, A. Walton, M. Bajdich, Z. Li, L. Lammich, A. Vojvodic, J. Lauritsen, *Nat. Commun.* **2017**, *8*, 14169.
[40] O. D. Pozo-Zamudio, S. Schwarz, M. Sich, I. A. Akimov, M. Bayer, R. C. Schofield, E. A. Chekhovich, B. J. Robinson, N. D. Kay, O. V. Kolosov, A. I. Dmitriev, G. V. Lashkarev, D. N. Borisenko, N. N. Kolesnikov, A. I. Tartakovskii, *2D Mater.* **2015**, *2*, 035010.
[41] a) Q. Zhao, T. Wang, Y. Miao, F. Ma, Y. Xie, X. Ma, Y. Gu, J. Li, J. He, B. Chen, S. Xi, L. Xu, H. Zhen, Z. Yin, J. Li, J. Ren, W. Jie, *Phys. Chem. Chem. Phys.* **2016**, *18*, 18719; b) E. G. Gillan, A. R. Barron, *Chem. Mater.* **1997**, *9*, 3037; c) C. J. Bae, J. McMahon, H. Detz, G. Strasser, J. Park, E. Einarsson, D. B. Eason, *AIP Adv.* **2017**, *7*, 035113.
[42] http://www.leonland.de/elements_by_price/en/list?sort=p (accessed: July 2022).
[43] a) Y. Fan, X. Ma, X. Liu, J. Wang, H. Ai, M. Zhao, *J. Phys. Chem. C* **2018**, *122*, 27803; b) S.-m. Tian, J. Meng, J. Huang, Q. X. Li, *Chin. J. Chem. Phys.* **2020**, *33*, 427.
[44] Z. Chen, S. Chu, J. Chen, H. Chen, J. Zhang, X. Ma, Q. Li, X. Chen, *Nano Energy* **2019**, *56*, 294.
[45] M. Ogita, N. Saika, Y. Nakanishi, Y. Hatanaka, *Appl. Surf. Sci.* **1999**, *142*, 188.
[46] Y. Liu, J. Parisi, X. Sun, Y. Lei, *J. Mater. Chem. A* **2014**, *2*, 9919.
[47] S. Akbar, P. Dutta, C. Lee, *Int. J. Appl. Ceram. Technol.* **2006**, *3*, 302.
[48] P. Giannozzi, S. Baroni, N. Bonini, M. Calandra, R. Car, C. Cavazzoni, D. Ceresoli, G. L. Chiarotti, M. Cococcioni, I. Dabo, A. Dal Corso, S. de Gironcoli, S. Fabris, G. Fratesi, R. Gebauer, U. Gerstmann, C. Gougoussis, A. Kokalj, L. Michele, L. Martin-Samos, N. Marzari, F. Mauri, R. Mazzarello, S. Paolini, A. Pasquarello, L. Paulatto, C. Sbraccia, S. Scandolo, G. Sclauzero, et al., *J. Phys.: Cond. Matt.* **2009**, *21*, 395502.
[49] a) J. P. Perdew, K. Burke, M. Ernzerhof, *Phys. Rev. Lett.* **1996**, *77*, 3865; b) V. Barone, M. Casarin, D. Forrer, M. Pavone, M. Sambi, A. Vittadini, *J. Comput. Chem.* **2009**, *30*, 934.
[50] G. D'Olimpio, S. Nappini, M. Vorokhta, L. Lozzi, F. Genuzio, T. O. Menteş, V. Paolucci, B. Gürbulak, S. Duman, L. Ottaviano, A. Locatelli, F. Bondino, D. W. Boukhvalov, A. Politano, *Adv. Funct. Mater.* **2020**, *30*, 2005466.
[51] H. J. Monkhorst, J. D. Pack, *Phys. Rev. B* **1976**, *13*, 5188.


© 2022 The Authors. Advanced Functional Materials published by Wiley-VCH GmbH

16163028, 2022, 41, Downloaded from https://onlinelibrary.wiley.com/doi/10.1002/adfm.202205923 by CNR GROUP II Istituto di Scienza dell', Wiley Online Library on [23/05/2024]. See the Terms and Conditions (https://onlinelibrary.wiley.com/terms-and-conditions) on Wiley Online Library for rules of use; OA articles are governed by the applicable Creative Commons License